Multimodal photodetectors with vacuum deposited perovskite bilayers

Keywords: photodetector, perovskite, vacuum deposition, broadband, narrowband

Lucía Martínez-Goyeneche,‡ Lidón Gil-Escrig,‡ Daniel Tordera, Cristina Roldán-Carmona, Henk J. Bolink, Michele Sessolo*

Instituto de Ciencia Molecular, Universidad de Valencia, C/ Catedrático J. Beltrán 2, 46980 Paterna, Spain. E-mail: michele.sessolo@uv.es

‡ These authors contributed equally to this work.

Color discrimination and selective wavelength photodetection are crucial for many imaging applications. The most common method to achieve a narrowband spectral response is the combination of optical bandpass filters with broadband photodetectors. However, these devices can only operate in narrowband mode. In this study, we developed a photodetector that operates in broadband and narrowband mode depending on the illumination side. To achieve bifunctional behavior, two perovskites with different bandgaps were integrated in the device, where one of them acts as an optical filter. Broadband response is obtained illuminating from the side of the lower bandgap perovskite, deposited on the transparent substrate. When light is shined through the top perovskite, the spectral response of the photodetector is determined by the bandgap energy difference of the two perovskites, in our case exhibiting a narrowband response with a full width at half maximum (FWHM) below 50 nm centered in the near-infrared (760 nm).

Metal halide perovskites are interesting materials in many optoelectronic applications due to their favorable physical properties, and for the possibility to deposit high quality thin films with simple and low temperature techniques. Perovskites are characterized by high charge mobility,[1,2] high optical absorption coefficient,[3] tunable and direct bandgap,[4,5] long charge diffusion length[6], and defect tolerance.[7,8] In view of these, metal halide perovskites have been used as active materials in several types of electronic devices such as solar cells,[9,10] light-emitting diodes,[11,12] lasers[13,14], and photodetectors.[15,16] While their main field of applications remains photovoltaics, they have increasingly been studied for photon and ionizing radiation detection.[17,18]

Photodetectors (PDs) are key components for applications such as image sensing, surveillance systems, optical communications, and intelligent monitoring.[19–23] If the photodetector is based on a semiconductor diode structure, it is called a photodiode.[24] When the electrical contacts are symmetric and/or not charge selective, photoconductors are obtained, which are also called photomultiplication-type photodetectors in view of their high gain.[25,26] Moreover, photodetectors are classified into two types according to their spectral responsivity bandwidth: broadband (sensitive to a broad spectrum of photon energy) and narrowband (able to detect selective photon energies and thus discriminate colors). Traditionally, narrowband photodetectors are obtained by combining broadband photodetectors with optical bandpass filters.[27–29] An alternative method to narrow the spectral response relies on a process called charge collection narrowing. In a thick junction, high energy photons are absorbed close to the surface, hence the photogenerated carriers will almost quantitatively recombine before reaching the external electrodes. However, low energy photons will be absorbed within the volume of the semiconductor, with much reduced recombination losses leading to a high photoresponse. Hence the spectral response of a thick diode is restricted in the bandgap region, where the absorption coefficient drops. This principle has been demonstrated in organic semiconductors and later also in perovskite films.[30–37] Saidaminov *et al.* used this principle in photodetectors based on a thick $MAPbI_3$ microcrystalline film, which operate in the broadband regime when illuminated from the indium tin oxide (ITO) side, and in the narrowband regime when illuminated from the air/perovskite interface. In this way, dual functional PDs were obtained (broad and narrowband), depending on the illumination side.[38] Recently, we have demonstrated a multilayer diode architecture which allowed for narrowband response due to the integration of a perovskite photoconductor (acting also as an optical filter) and a perovskite photodiode.[39] This configuration is enabled by the use of vacuum deposition methods, which allow the fabrication of multilayer structures.

In this work, we fabricated a dual mode photodetector that can operate in both broadband and narrowband mode depending on the illumination conditions (under bottom and top illumination, respectively). In particular, we deposited methylammonium lead iodide (MAPI, 1.6 eV) on patterned interdigitated ITO glass substrate and subsequently deposited a wide bandgap (1.70 eV) $FA_{0.7}Cs_{0.3}Pb(I_{0.7}Br_{0.3})_3$ perovskite on top that acts as an optical filter. The perovskite films are separated by a metal oxide layer, which is needed to prevent intermixing of the two perovskites due to ion diffusion. When illuminated through the glass side, the PD shows the typical broadband response of thin-film semiconductors diodes. However, the PDs have a narrow spectral response under top illumination, centered in the near-infrared (NIR, 760 nm) and with a full width at half maximum (FWHM) of approximately 50 nm.

We fabricated lateral photodetectors by depositing the perovskite films directly on ITO interdigitated electrodes (with a spacing of 50 μm) on glass substrates. This photodetector configuration is widely adopted due to the simplicity of the fabrication process, although it compromises the response speed and require high driving voltages.[15,40,41] The PDs are composed of two perovskite films: first, MAPI (500 nm thick) is deposited directly on the substrate, and then it is coated with a wider bandgap perovskite of the type $FA_{0.65}Cs_{0.35}Pb(I_{0.73}Br_{0.27})_3$ (1 μm thick, in the following: CsFAPbIBr). All layers are deposited by thermal vacuum deposition following previously reported protocols,[42,43] and as described in the experimental section. In order to avoid spontaneous halide interdiffusion between the two perovskite films, we tested the use of an alumina layer in between the two films, which was deposited by atomic layer deposition (ALD).[44] The same ALD layer was used as an envelope encapsulation layer after the deposition of the second perovskite film. Fig. 1 shows images of the cross-section scanning electron microscopy (SEM) and energy dispersive spectroscopy (EDS) analysis of the photodetectors. The images were taken 48 hours after the device preparation, and the photodetectors were stored in dry nitrogen atmosphere prior to the SEM analysis. Grains of the $FA_{0.65}Cs_{0.35}Pb(I_{0.73}Br_{0.27})_3$ surface film present the same appearance for both photodetectors (Fig. S1). The bare MAPI/CsFAPbIBr bilayer shows a homogeneous structure in the cross-section (Fig. 1a), with the presence of smaller grains on the bottom of the device, where MAPI perovskite is deposited. By looking at the elemental distribution across the MAPI/CsFAPbIBr bilayer, we observed that bromide is homogeneously distributed through the whole section of the device (Fig. 1b), in a similar fashion as Pb (Fig. 1c). The oxygen signal (Fig. 1d) is shown here as a reference to identify the buried ITO/perovskite interface. This observation indicates spontaneous halide intermixing at room temperature.

Clark *et al.* proved mixing between perovskite/perovskite layers depends on chemical composition and grain size, identifying which species diffuse across the interface and the mixing rate[45]. In our device, Br was detected across the thickness of both perovskites which indicates the ion transport resulting in a mixing perovskite. Another potentially interesting element here is Cs, however, the signal was comparable to the detection limits of the instrument.

When a 30 nm thick Al_2O_3 layer is introduced in the device stack between both perovskites, the MAPI/FACsPbIBr bilayer can be clearly distinguished in the cross-sectional SEM image (Fig. 1e), thanks to the different morphology and contrast of the two perovskite films. Importantly, as Fig. 1f illustrates, bromine is only detected on top of Al_2O_3 layer, and originates solely from the wide band gap perovskite CsFAPbIBr. Note that the brighter areas below and on top of the CsFAPbIBr film in the Br map are due to the presence of Al (from the two Al_2O_3 layers used as diffusion barrier in between the perovskites and as encapsulation), as the EDS photon energy for Br and Al coincides. The Pb and O signals further confirm the presence of two separated perovskite films (Fig. 1g-h), as seen from the dark line in the Pb map and the O blue line in the O map between the perovskites films, both corresponding to the Al_2O_3 interlayer.

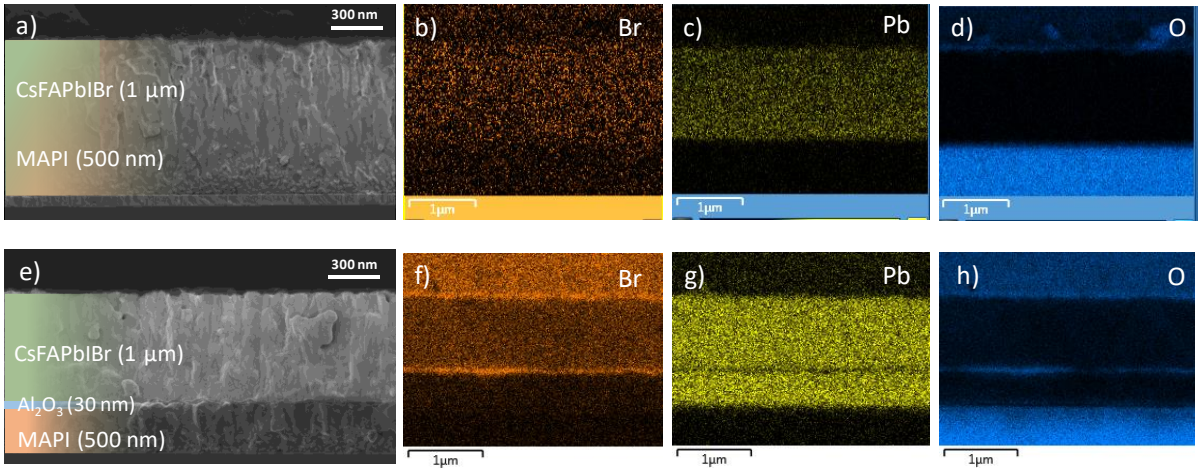

Fig. 1 (a) Cross-sectional SEM image of the MAPI/CsFAPbIBr bilayer device with (b-d) the corresponding EDS maps for selected elements: (b) Br, (c) Pb and (d) O. (e) Cross-sectional SEM image of the MAPI/Al_2O_3/CsFAPbIBr device with (f-h) the corresponding EDS maps for selected elements: (f) Br, (g) Pb and (h) O.

We measured the spectral response of the devices under an applied electrical bias, illuminating the devices from the bottom (through the MAPI layer) and from the top (through the CsFAPbIBr layer). Fig. 2a shows the external quantum efficiency (EQE) recorded at an applied bias of 5 V for the MAPI/CsFAPbIBr bilayer photodetector, illuminated from top and bottom. As a consequence of the halide interdiffusion, the device shows a similar broadband spectral response regardless of the illumination side. The EQE values are comparable, with a small shift in the bandgap depending on the illumination side (the bandgap is estimated from the maximum in the first derivative of the EQE spectrum, Fig. 2b). With top illumination the bandgap estimated from EQE is slightly higher compared to the same measurement using bottom illumination (1.635 eV and 1.630 eV respectively). Both values differ from the bandgap of the two isolated perovskite films, 1.60 and 1.70 eV for MAPI and CsFAPbIBr, respectively.[46,47] The bandgap values agree also with the PL spectra collected by exciting the MAPI/CsFAPbIBr bilayer from the bottom and the top (Fig. S2a), with maxima at 751 and 744 nm, respectively. Albeit small, the different bandgaps observed from top and bottom illumination likely originate from a residual gradient in the bromide content, which is not completely and evenly distributed through the film cross-section.

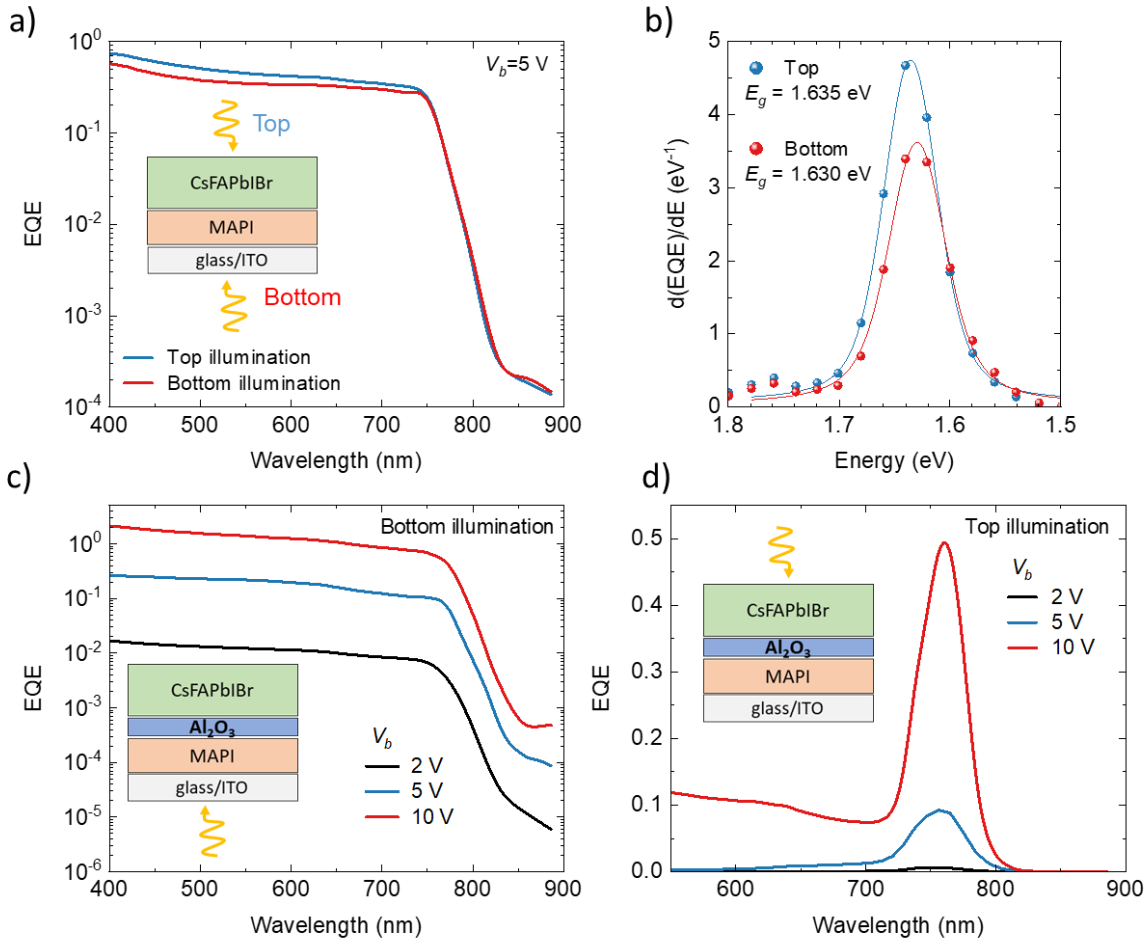

Fig. 2 External quantum efficiency (EQE) characterization of bilayers PDs. (a) EQE spectra of the ITO/MAPI/CsFAPbIBr device upon illumination from the top (blue line) and bottom (red line). (b) First derivative of the EQE spectrum fitted with a Voigt function to determine the peak center, corresponding to the energy bandgap (blue and red indicates top and bottom illumination, respectively). EQE spectra of the dual mode ITO/MAPI/Al_2O_3/CsFAPbIBr photodetector when illuminated from the (c) bottom and (d) and top at different applied voltage bias.

On the contrary, the PL spectra of the ITO/MAPI/Al_2O_3/CsFAPbIBr photodetector (Fig. S2(b)) present two different peaks depending on the illumination side, that corresponds to the luminescence of each perovskite. This further indicates that no intermixing takes place with the ALD barrier layer. Hence, we characterized the spectral response of the

MAPI/Al_2O_3/CsFAPbIBr photodetector, first by measuring the EQE spectrum from the substrate (bottom) side (Fig. 2c). We observed a broadband response in the EQE from 400 nm to 800 nm, approximately, corresponding to the expected response from a MAPI film. The corresponding energy bandgap was estimated to be 1.60 eV (Fig. S3), in agreement with previous reports on vacuum deposited MAPI.[46] The maximum EQE values were found to increase with the applied voltage from 2% to 26% and to 210% (corresponding to a responsivity of 5.4 mA/W, 45 mA/W and 676 mA/W, see Fig. S4a), when the applied bias was 2 V, 5 V and 10 V, respectively. The over unity EQE results from photoconductive gain, which is a consequence of trapped charges allowing the charge of opposite sign to circulate several times before recombining.[16,38,48–51] The EQE spectrum of the photodetector measured from the top side is reported in Fig. 2d. We observed a narrow peak in the EQE centered at 760 nm. The narrowband spectral response is due to the use of CsFAPbIBr perovskite as a filter: the CsFAPbIBr film absorbs above-bandgap photons leaving only light with energy below its bandgap to reach the MAPI perovskite. Considering the bandgap of the two perovskites, the wavelength difference in the EQE spectral response is expected to be approximately 46 nm. This value agrees with the full width at half maximum (FWHM) of the EQE peak, which varies from 42 to 48 nm depending on the applied bias voltage, and is comparable to best-in-class narrowband perovskite PDs in the near-infrared regime.[29,52–54] At the maximum of the response band, the EQE values are 0.7% at 2 V, 9% at 5 V and 48% at 10 V (the corresponding responsivity spectra are reported in Fig. S4b).

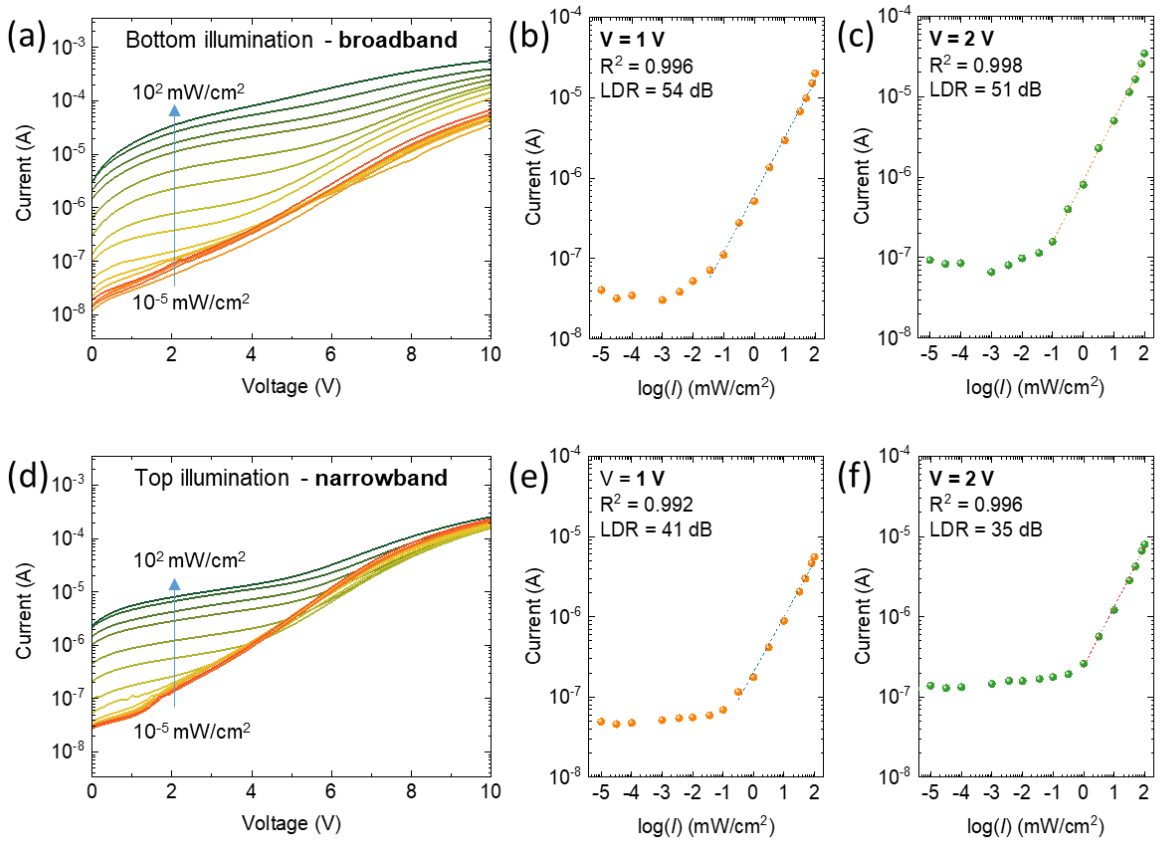

Fig. 3 Optoelectronic characterization of the dual mode photodetector under increasing illumination intensity (*I*). (a) I-V characteristics and corresponding response versus light intensity at (b) 1 V and (c) 2 V when the photodetector is illuminated from the bottom (through the MAPI film). (d) I-V characteristics and corresponding response versus light intensity at (e) 1 V and (f) 2 V when the photodetector is illuminated from the top (through the CsFAPbIBr film). The LDR is obtained by fitting the linear part of the light response.

We collected the current-voltage (I-V) characteristics of the MAPI/Al_2O_3/CsFAPbIBr photodiode under bottom and top side illumination, in order to quantify the sensor response in both the broadband and narrowband regime, respectively (Fig. 3). The light intensity was tuned over 7 orders of magnitude from 100 mW/cm^2 down to 10^{-5} mW/cm^2 using an LED solar simulator in combination with neutral density filters. Under both illumination modes (bottom and top), the MAPI perovskite generates charge carriers at the vicinity of the ITO interdigitated electrodes, which results in a net photocurrent in both cases (Fig. 3a and 3d). However, in narrowband mode (with top illumination), the overall photocurrent of the detector is lower due to the optical absorption of the CsFAPbIBr perovskite used as a filter (Fig. 3d). When tuning

the illumination intensity 7 order of magnitudes, we observe a change in the photocurrent of approximately 2 and 3 orders of magnitude (at low applied voltage), for the device in narrowband and broadband response, respectively. We quantified the linear dynamic range (LDR) of the dual-mode MAPI/Al_2O_3/CsFAPbIBr detector at an applied bias of 1 and 2 V, where the signal-to-noise ratio is larger. The LDR was estimated using the relation LDR = 20 · log ($I_{ph,max}/I_{ph,min}$), where $I_{ph,max}$ and $I_{ph,min}$ are the photocurrent measured at the two extremes (maximum and minimum) of the linear part of the detector response. In the broadband mode (bottom illumination, Fig. 3b-c), the LDR of the device is 54 dB and 51 dB at 1 V and 2 V applied bias, respectively. Due to the lower photocurrent, the LDR in narrowband mode (top illumination, Fig. 3e-f) is reduced to 41 dB and 35 dB at 1 V and 2 V, respectively. The LDR is reduced at higher voltage due to the fact the photocurrent does not follow the dark current trend with increasing applied bias. Due to the narrow spectral response, the photocurrent in the narrowband mode is small, and comparable to the dark current at high driving voltage. The rather high dark current in the device is characteristic of photoconductive devices, in turn limiting the LDR and detectivity of the detector.[15] When estimating the specific detectivity at 5V applied bias, the bilayer device shows a maximum of $2 \cdot 10^9$ Jones in the broadband mode and of 10^9 Jones at the spectral response peak in narrowband mode (Fig. S4c-d), three order of magnitude lower compared to narrowband photodiode with similar device concept.[39] Nevertheless, the simple bilayer perovskite photodetector is capable of discriminating light with an intensity as low as 0.1 mW/cm^2 in broadband mode, and 1 mW/cm^2 in the narrowband mode. We also investigated the photodetector response speed to short laser pulses (Fig. S5), and measured a rise time of 570 ns, and a larger fall time of 1.180 µs, which is only slightly larger (a factor of 2) than multilayer perovskite narrowband photodiodes.[29] Further studies will be carried out in order to enhance the narrowband response of these detectors, in order to achieve photoconductive gain while maintaining a high color selectivity.

Conclusion

We show a new concept to obtain dual mode perovskite photodetectors that can operate as broadband and narrowband light sensors depending on the illumination side. Using vacuum deposition techniques, we fabricated simple bilayer devices composed of two perovskites, $MAPbI_3$ and a wider bandgap perovskite, $Cs_{0.3}FA_{0.7}Pb(I_{0.7}Br_{0.3})_3$, where the latter is processed on top of $MAPbI_3$. In order to avoid intermixing of the two perovskites, consequence of ion diffusion, we used an alumina barrier layer in between the two materials. When illuminated from the top side, the CsFAPbIBr perovskite act as a filter and allows only low energy photons

to be absorbed and converted to a photocurrent by the $MAPbI_3$ layer, leading to narrowband response. On the other hand, when illuminated from the bottom side, the device shows the expected broadband spectral response of the direct bandgap $MAPbI_3$ semiconductor. The dual-mode photodetector shows a broad spectral response from 400 nm to 800 nm under bottom illumination, and a narrow spectral response when illuminated from the top, with a peak centered in the near-infrared (760 nm) and with a full width at half maximum (FWHM) <50 nm.

Experimental

Materials and chemicals

Formamidinium iodide (FAI) was purchased from Greatcell Solar, methylammonium iodide (MAI), lead iodide (PbI_2) and bathocuproine (BCP) were purchased from Luminescence Technology Corp. Lead bromide ($PbBr_2$) was obtained from Tokyo Chemical Industry. Trimethylaluminum (electronic grade, 99.99%) was purchased from Strem Chemicals.

Device fabrication

Pre-patterned ITO-coated glass substrates were subsequently cleaned with soap, water and isopropanol in an ultrasonic bath, followed by a 20 min UV-ozone treatment. Substrates were transferred to a vacuum chamber integrated in a nitrogen-filled glovebox and evacuated to a pressure of 10^{-6} mbar. For $MAPbI_3$ deposition, MAI and PbI_2 were co-evaporated simultaneously with rates of 0.6 Å/s and 1 Å/s, respectively. Two evaporation sources (one for PbI_2 and one for MAI) and three QCM sensors were used for $MAPbI_3$ deposition, where two controlled the deposition rate of the sources and the third one (close to the substrate holder) was used to monitor the total deposition rate. During the evaporation the pressure of the chamber was maintained at $5 \cdot 10^{-6}$ mbar. The $FA_{0.7}Cs_{0.3}Pb(I_{0.7}Br_{0.3})_3$ perovskite was evaporated in a vacuum chamber equipped with four evaporation sources (Creaphys) and with independent temperature controllers, shutter and QCM sensor, following a previously reported protocol[47]. For both the alumina interlayer and encapsulation, Al_2O_3 (30 nm) was deposited by atomic layer deposition in an Arradiance reactor at 40 °C, using a previously published protocol.[44]

Device characterization

The photoluminescence spectra were measured with an Avantes Avaspec2048 spectrometer where films were illuminated with a diode laser from Integrated Optics, emitting at 515 nm. The spectra were collected with integration times of 1 s. The *I-V* curves were recorded with a

Keithley 2612A SourceMeter in a 0 and 10 V voltage range with 0.1 V steps and the devices were illuminated with a Wavelabs Sinus 70 LED solar simulator using a custom LabVIEW program. The light intensity was calibrated before every measurement using a calibrated Si reference diode. Intensity dependent data were carried out by measuring *I-V* curves in the same system using neutral density filters of decreasing optical density. In the EQE measurements the devices were illuminated with a Quartz-Tungsten-Halogen lamp (Newport Apex 2-QTH) through a monochromator (Newport CS130-USB-3-MC), a chopper at 77 Hz and a focusing lens. The device current was measured as a function of energy from 3.5 eV to 1.5 eV in 0.05 eV steps and from 2.4 eV to 1.4 eV in 0.02 eV steps using a lock-in amplifier (Stanford Research Systems SR830). The SEM images were taken with a Field Emission Scanning Electron Microscope (HR-FESEM), ZEISS GeminiSEM 500 model, with a secondary Electron In-Lens detector using an accelerating voltage of 0.7-1 kV. The EDS images were obtained using the same equipment provided with an X-Ray Dispersive Energy Detector (Oxford Instruments).

Conflicts of interest

There are no conflicts to declare.

Acknowledgements

We acknowledge the Electron Microscopy Service of the Universitat Politècnica de València for technical assistance with the SEM and EDS analysis. We acknowledge support from the Comunitat Valenciana (PROMETEU/2020/077, CIGE/2021/027 and CISEJI/2022/43), the Ministry of Science and Innovation (MCIN) and the Spanish State Research Agency (AEI): Project PCI2020-112084 and grant IJCI-2019-039851-I funded by MCIN/AEI/10.13039/501100011033 and by the "European Union NextGenerationEU/PRTR"; Grants PRE2019-091181 and RYC-2016-21316 funded by MCIN/AEI/10.13039/501100011033 and by "ESF Investing in your future"; Grant CEX2019-000919-M funded by MCIN/AEI/10.13039/501100011033.

References

1 L. M. Herz, *ACS Energy Lett.*, 2017, **2**, 1539–1548.

2 C. Motta, F. El-Mellouhi and S. Sanvito, *Sci. Rep.*, 2015, **5**, 12746.

3 G. Xing, N. Mathews, S. Sun, S. S. Lim, Y. M. Lam, M. Grätzel, S. Mhaisalkar and T. C. Sum, *Science (80-.).*, 2013, **342**, 344–347.

4 L. Protesescu, S. Yakunin, M. I. Bodnarchuk, F. Krieg, R. Caputo, C. H. Hendon, R. X. Yang, A. Walsh and M. V. Kovalenko, *Nano Lett.*, 2015, **15**, 3692–3696.

5 S. a. Kulkarni, T. Baikie, P. P. Boix, N. Yantara, N. Mathews and S. Mhaisalkar, *J. Mater. Chem. A*, 2014, **2**, 9221.

6 S. D. Stranks, G. E. Eperon, G. Grancini, C. Menelaou, M. J. P. Alcocer, T. Leijtens, L. M. Herz, A. Petrozza and H. J. Snaith, *Science (80-.).*, 2013, **342**, 341–344.

7 W. Chu, Q. Zheng, O. V. Prezhdo, J. Zhao and W. A. Saidi, *Sci. Adv.*, 2020, **6**, eaaw7453.

8 G. Kim and A. Petrozza, *Adv. Energy Mater.*, 2020, **10**, 2001959.

9 N.-G. Park, *J. Phys. Chem. Lett.*, 2013, **4**, 2423–2429.

10 C. Zhang, T. Shen, D. Guo, L. Tang, K. Yang and H. Deng, *InfoMat*, 2020, **2**, 1034–1056.

11 X. K. Liu, W. Xu, S. Bai, Y. Jin, J. Wang, R. H. Friend and F. Gao, *Nat. Mater.*, 2021, **20**, 10–21.

12 A. Fakharuddin, M. K. Gangishetty, M. Abdi-Jalebi, S.-H. Chin, A. R. bin Mohd Yusoff, D. N. Congreve, W. Tress, F. Deschler, M. Vasilopoulou and H. J. Bolink, *Nat. Electron.*, 2022, **5**, 203–216.

13 Q. Zhang, R. Su, W. Du, X. Liu, L. Zhao, S. T. Ha and Q. Xiong, *Small Methods*, 2017, **1**, 1700163.

14 G. Xing, N. Mathews, S. S. Lim, N. Yantara, X. Liu, D. Sabba, M. Grätzel, S. Mhaisalkar and T. C. Sum, *Nat. Mater.*, 2014, **13**, 476–480.

15 H. Wang and D. H. Kim, *Chem. Soc. Rev.*, 2017, **46**, 5204–5236.

16 M. Ahmadi, T. Wu and B. Hu, *Adv. Mater.*, 2017, **29**, 1605242.

17 H. Wei and J. Huang, *Nat. Commun.*, 2019, **10**, 1066.

18 A. Datta, B. Barman, S. Magill and S. Motakef, *Sci. Rep.*, 2020, **10**, 16932.

19 F. P. García de Arquer, A. Armin, P. Meredith and E. H. Sargent, *Nat. Rev. Mater.*, 2017, **2**, 16100.

20 G. Konstantatos and E. H. Sargent, *Nat. Nanotechnol.*, 2010, **5**, 391–400.

21 G. Simone, M. J. Dyson, S. C. J. Meskers, R. A. J. Janssen and G. H. Gelinck, *Adv. Funct. Mater.*, , DOI:10.1002/adfm.201904205.

22 C. Li, Y. Ma, Y. Xiao, L. Shen and L. Ding, *InfoMat*, 2020, **2**, 1247–1256.

23 X. Huang, Y. Guo and Y. Liu, *Chem. Commun.*, 2021, **57**, 11429–11442.

24 C. Li, Y. Ma, Y. Xiao, L. Shen and L. Ding, *InfoMat*, 2020, **2**, 1247–1256.

25 K. Yang, Z. Zhao, M. Liu, L. Niu, X. Zhao, G. Yuan, X. Ma and F. Zhang, *J. Mater. Chem. C*, 2022, **10**, 10888–10894.

26 S. Xing, J. Kublitski, C. Hänisch, L. C. Winkler, T. Li, H. Kleemann, J. Benduhn and K. Leo, *Adv. Sci.*, 2022, **9**, 2105113.

27 G. Yu, J. Wang, J. McElvain and A. J. Heeger, *Adv. Mater.*, 1998, **10**, 1431–1434.

28 M. Dandin, P. Abshire and E. Smela, *Lab Chip*, 2007, **7**, 955–977.

29 L. Li, Y. Deng, C. Bao, Y. Fang, H. Wei, S. Tang, F. Zhang and J. Huang, *Adv. Opt. Mater.*, 2017, **5**, 1700672.

30 A. Armin, R. D. Jansen-van Vuuren, N. Kopidakis, P. L. Burn and P. Meredith, *Nat. Commun.*, 2015, **6**, 6343.

31 H.-S. Rao, W.-G. Li, B.-X. Chen, D.-B. Kuang and C.-Y. Su, *Adv. Mater.*, 2017, **29**, 1602639.

32 G. Maculan, A. D. Sheikh, A. L. Abdelhady, M. I. Saidaminov, M. A. Haque, B. Murali, E. Alarousu, O. F. Mohammed, T. Wu and O. M. Bakr, *J. Phys. Chem. Lett.*, 2015, **6**, 3781–3786.

33 J. Li, J. Wang, J. Ma, H. Shen, L. Li, X. Duan and D. Li, *Nat. Commun.*, 2019, **10**, 806.

34 J. Zhou, J. Luo, X. Rong, P. Wei, M. S. Molokeev, Y. Huang, J. Zhao, Q. Liu, X. Zhang, J. Tang and Z. Xia, *Adv. Opt. Mater.*, 2019, **7**, 1900139.

35 P. Zhang, Y. Hua, X. Li, L. Zhang, L. Liu, R. Li, G. Zhang and X. Tao, *J. Mater. Chem. C*, 2021, **9**, 2840–2847.

36 J. Zhao, X. Wang, Y. Xu, Y. Pan, Y. Li, J. Chen, Q. Li, X. Zhang, Z. Zhu, Z. Zhao, E. E. Elemike, D. C. Onwudiwe, B. S. Bae, S. Bin Shafie and W. Lei, *ACS Appl. Mater. Interfaces*, 2022, **14**, 25824–25833.

37 M. Liu, J. Wang, Z. Zhao, K. Yang, P. Durand, F. Ceugniet, G. Ulrich, L. Niu, Y. Ma, N. Leclerc, X. Ma, L. Shen and F. Zhang, *J. Phys. Chem. Lett.*, 2021, **12**, 2937–2943.

38 M. I. Saidaminov, M. A. Haque, M. Savoie, A. L. Abdelhady, N. Cho, I. Dursun, U. Buttner, E. Alarousu, T. Wu and O. M. Bakr, *Adv. Mater.*, 2016, **28**, 8144–8149.

39 L. Martínez-Goyeneche, L. Gil-Escrig, I. Susic, D. Tordera, H. J. Bolink and M. Sessolo, *Adv. Opt. Mater.*, 2022, **10**, 2201047.

40 J. Miao and F. Zhang, *J. Mater. Chem. C*, 2019, **7**, 1741–1791.

41 T. Yang, F. Li and R. Zheng, *ACS Appl. Electron. Mater.*, 2019, **1**, 1348–1366.

42 C. Momblona, L. Gil-Escrig, E. Bandiello, E. M. Hutter, M. Sessolo, K. Lederer, J. Blochwitz-Nimoth and H. J. Bolink, *Energy Environ. Sci.*, 2016, **9**, 3456–3463.

43 D. Pérez-del-Rey, L. Gil-Escrig, K. P. S. Zanoni, C. Dreessen, M. Sessolo, P. P. Boix and H. J. Bolink, *Chem. Mater.*, , DOI:10.1021/acs.chemmater.9b01396.

44 I. C. Kaya, K. P. S. Zanoni, F. Palazon, M. Sessolo, H. Akyildiz, S. Sonmezoglu and H. J. Bolink, *Adv. Energy Sustain. Res.*, 2021, **2**, 2000065.

45 C. P. Clark, J. E. Mann, J. S. Bangsund, W.-J. Hsu, E. S. Aydil and R. J. Holmes, *ACS Energy Lett.*, 2020, **5**, 3443–3451.

46 F. Palazon, D. Pérez-del-Rey, B. Dänekamp, C. Dreessen, M. Sessolo, P. P. Boix and H. J. Bolink, *Adv. Mater.*, 2019, **31**, 1902692.

47 L. Gil-Escrig, C. Dreessen, F. Palazon, Z. Hawash, E. Moons, S. Albrecht, M. Sessolo and H. J. Bolink, *ACS Energy Lett.*, 2021, **6**, 827–836.

48 A. Pierre and A. C. Arias, *Flex. Print. Electron.*, 2016, **1**, 043001.

49 H. Wang, S. Li, X. Liu, Z. Shi, X. Fang and J. He, *Adv. Mater.*, 2021, **33**, 2003309.

50 R. Dong, Y. Fang, J. Chae, J. Dai, Z. Xiao, Q. Dong, Y. Yuan, A. Centrone, X. C. Zeng and J. Huang, *Adv. Mater.*, 2015, **27**, 1912–1918.

51 X. Zhao, L. Huang, Y. Wang, X. Zhu, L. Li, G. Li and W. Sun, *RSC Adv.*, 2020, **10**, 32976–32983.

52 Z. Lan, L. Cai, D. Luo and F. Zhu, *ACS Appl. Mater. Interfaces*, 2021, **13**, 981–988.

53 Z. Liu, L. Tao, Y. Zhang, G. Zhou, H. Zhu, Y. Fang, G. Wu, D. Yang and H. Chen, *Adv. Opt. Mater.*, 2021, **9**, 2100288.

54 S. Liu, N. Ding, Y. Wu, L. Zi, Y. Wang, J. Hu, T. Xie, D. Zhou, X. Bai, W. Xu and H. Song, *J. Phys. Chem. Lett.*, 2022, **13**, 6057–6063.